The definitive version of this article is published as:
J. Chen;S. J. Bull. Indentation fracture and toughness assessment for thin optical coatings on glass. *Journal of Physics D-Applied Physics* 2007, 40(18), 5401-5417.

# Indentation fracture and toughness assessment for thin optical coatings on glass

J. Chen and S.J. Bull
Department of Chemical Engineering and Advanced Materials
University of Newcastle Upon Tyne
NE1 7RU, UK

**Abstract**

Different indentation fracture mechanisms of coated glass caused by a sharp tip (cube corner) at low loads (<4mN) and a blunt tip (Berkovich) at high loads (up to 500mN) have been analysed in this study. The existing indentation methods to estimate the fracture toughness are unsuitable for investigating very thin coatings (<500nm). An alternative energy-based method can successfully be applied in the assessment of the ultra-small cracks produced in coated glass based on excursions in the load-displacement curve caused by sharp indentation. However, it was found that no excursions were observed associated with picture frame cracks produced by the blunt tip in the same coatings; this is not unusual in other coated systems which makes the existing energy-based models invalid. Therefore, a new energy-based model is developed here to solve this problem and good results have been obtained. The existing models cannot be applied to the analysis of the indentation-induced interfacial failure in this study, therefore, new approaches have also been developed to assess the interfacial toughness and again reasonable results are obtained.

Key words: Fracture, toughness, coatings, adhesion, nanoindentation

## 1. Introduction

Multilayer metal/oxide coating systems have been applied in a range of applications including, microelectronics, microelectromechanical systems (MEMS) and optics; for instance, solar control coatings consisting of a selective absorbing layer, antireflection layers and barrier layers on glass are used in architectural applications in order to save energy. Whatever the application, the coating lifetime is a key issue that needs to be addressed This is often controlled by the mechanical properties of the coated system, particularly where coated components are handled or assembled, and it is therefore important to understand the fracture mechanisms during contact.

The fracture of a coated system is not only dependent on coating toughness and the distribution of flaws, but may also depend on the properties of the substrate and interface. Fracture mechanisms of coated systems composed of thick hard coatings on soft substrates have been well-documented in the literature [1-3]. However, research on the fracture mechanisms of thin hard coatings (<500nm) on hard substrates is less well-established. In this paper, the fracture mechanisms of ceramic optical coatings on

glass are highlighted to illustrate the new methods developed to extract fracture toughness information for the coatings. Traditional indentation fracture assessment is mainly based on the analysis of radial cracks, ring cracks and chipping in thick coatings [3-6]. Here, an analysis based on picture-frame cracking in coated glass is developed to generate fracture toughness information and this is compared with an alternative energy-based method based on the analysis of nanoindentation load-displacement curves. In addition, the use of such curves to assess the interfacial toughness of very thin coatings is discussed.

## 2. Brief review of the indentation methods to assess fracture toughness

For a well-developed halfpenny-like (semi-circular) median/radial cracking caused by indentation (Figure 1) which was observed by viewing transparent materials from the side during indentation [7,8], the toughness $K_{Ic}$ is related to applied load, $P$, and crack length, $c$, as follows.

$$K_{Ic} = \chi P / c^{3/2} = \xi_v^R (E/H)^{1/2} P / c^{3/2} \quad (1)$$

where $\xi_v^R$ is a calibration coefficient which depends on indenter geometry and crack pattern and E and H are Young's modulus and hardness, respectively. For well developed radial cracking produced by a Vickers indenter, $\xi_v^R$=0.016±0.004 [7,9]. With a decrease of the indenter semi-angle, θ, $\xi_v^R$ increases since it is proportional to $(\cot\theta)^{2/3}$. This was derived based on the expanding cavity model [7] and was verified by indentation in different brittle materials [10]. The geometry-dependent behaviour has been verified for tip angles in the range of 35.3 ° to 75 ° [10].

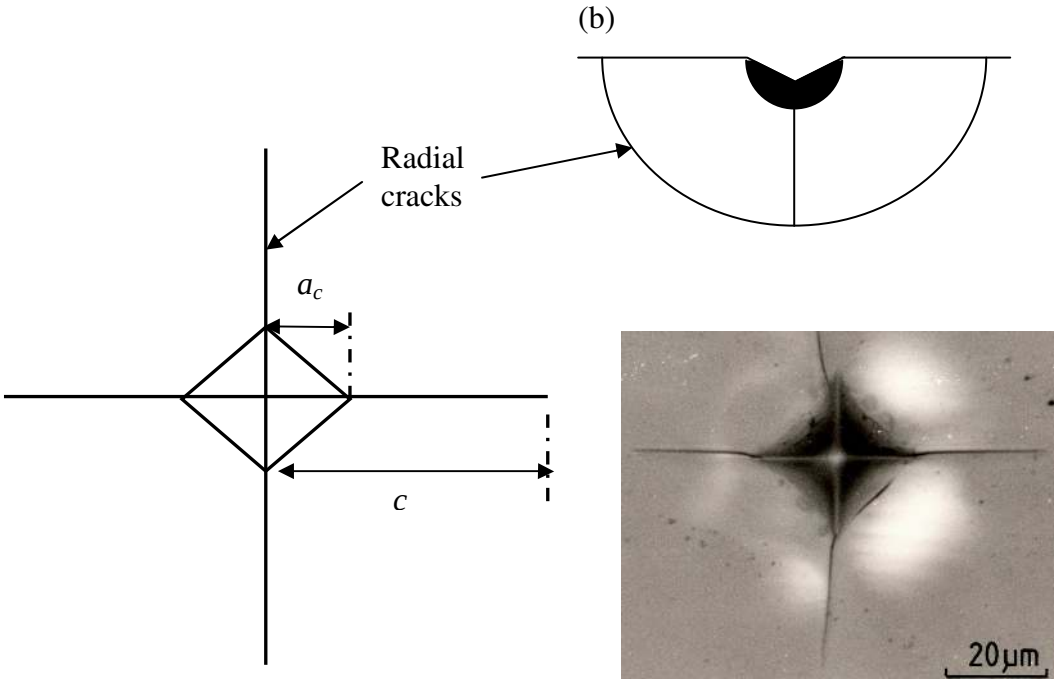


(a) (c)

**Figure 1.** Schematic of well developed radial cracking caused by indentation in a brittle material with a Vickers indenter, (a) top view and (b) side view. (c) Radial cracking in glass.

The simplicity and reliability of this technique makes it a common method to extract the fracture toughness for bulk materials indented at high loads. The influence of residual stress can also be considered for bulk materials and thick coatings in this model [4, 11–13]. However, when the coating thickness decreases, well-developed radial cracking may not be observed (e.g. for 400nm Solar control coatings on glass in [14] and 500nm $SiO_2$ filled methyltrimethoxysilane coatings on glass in [12]). In such cases, the utility of the above equations will be in doubt. For example, Laugier [15] and Nihara et al [16] reported that the linear relationship between $K_{Ic}$ and $P/c^{3/2}$ broke down when $c<2.5a_c$ (where $a_c$ is the contact radius of the impression as depicted in Fig. 1). However, Jang et al [10] argued that such a scaling relationship is still maintained even for small cracks in Si (100) and Scholz et al [17] found that such a scaling relationship remained even when the radial crack length was down to $1.1a_c$ for typical ceramics such as fused silica and sapphire.

For a cube corner tip several researchers have reported different values of the coefficient $\xi_v^R$ in Eq.(1). If it is assumed that $\xi_v^R$ is related to tip angle only ($\xi_V^R = \xi_r^R(\cot\theta)^{\frac{2}{3}}$, where $\xi_r^R$ is a constant), it can be expected to have a value of 0.033; however, 0.0319 [18], 0.036 [19] , 0.04 [20], and 0.0535[21] have been reported as different values for the constant. This has been critically discussed in [22]. This model has been generalized and extended by considering the wedging stress in brittle bulk materials [23,24]. However, with the decrease of coating thickness, the deformation of substrate will not only significantly affect the fracture morphology in coatings but also the fracture mechanisms. Given these problems, energy based models have been proposed as alternatives, particularly now that routine measurement of indentation load-displacement curves allows direct calculation of the dissipated energy.

A widely used energy-based model was initially proposed by Li et al [5-6] based on extrapolating the loading curve when there is a step associated with through-thickness fracture in it. In this model the load-displacement curve is extrapolated from the step start point (assumed to be the onset of fracture) to its end point, and the difference between the extrapolated curve and the measured curve is regarded as the fracture dissipated energy. For convenience, this method will be denoted as the ld-dp method in this paper. The fracture toughness is related to the released elastic strain energy during fracture, $U$, the film thickness, $t$, the total length of the crack in the film plane $2\pi C_R$, Young's modulus of the film, $E$, and Poisson's ratio of the film, $\nu$, and it is given by,

$$K_{IC} = \left[\left(\frac{E}{(1-\nu^2)2\pi C_R}\right)\left(\frac{U}{t}\right)\right]^{1/2} \tag{2}$$

Later this was slightly modified by den Toonder et al by considering the effective coating thickness and the number of cracks [4].

However, through thickness fracture may change the stress field around the indenter and thus change the elastic-plastic behaviour of the coated system. This influence has been completely ignored in this model. The coating cannot survive to the extrapolated load and during the fracture event the indenter still does work which is mainly dissipated by elastic-plastic deformation. It was also argued elsewhere [4] that the area ACD in Fig. 2 is not the actual energy dissipated by fracture. Therefore, this model has been further developed by Chen and Bull [14] based on analysing the total work versus displacement curve ($W_t$-dp method). The method to determine fracture dissipated energy is explained in Figure 3. First, the initial $W_t$-dp curve is extrapolated from the cracking start point A to the cracking end point C, to get the work difference CD after fracture; then the $W_t$-dp curve after cracking is extrapolated backward to the cracking start point thus obtaining the work difference AB at the onset of fracture. AB represents the work caused by different elastic-plastic deformation behaviour of the material before and after fracture whereas CD represents the total work difference caused by the presence of cracking which consists of the change of elastic-plastic deformation behaviour between the uncracked system and cracked system plus the fracture dissipated energy (not including contribution from relaxation of residual stress in the coating). The difference between the two (i.e. CD minus AB in Fig.3) will be the fracture dissipated energy. This method has been successfully applied in many different coated systems [22, 25].

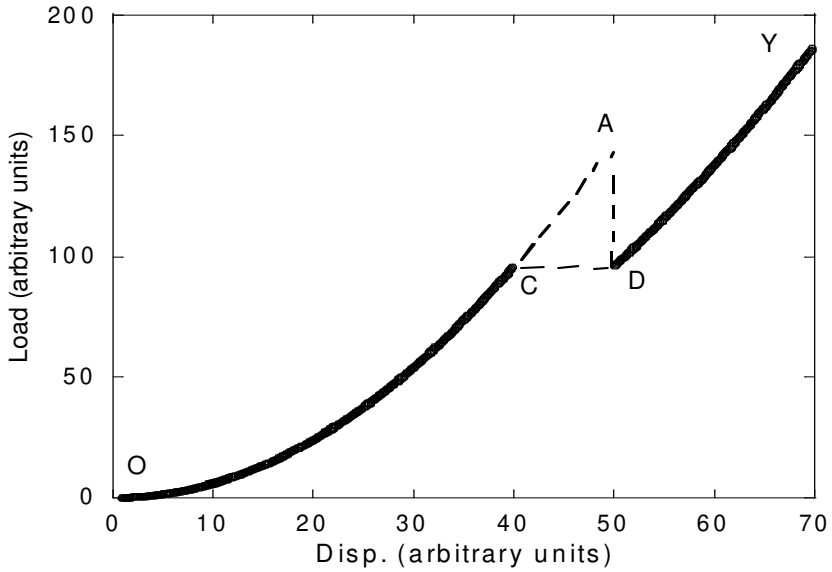


**Figure 2.** Schematic of the ld-dp method to determine the fracture dissipated energy, i.e. area ACD. See text.

An alternative energy based model was proposed by Malzbender and de With [26] based on plotting the irreversible work $W_{irr}$ over the total work done by indenter $W_t$ at a range of loads. This method requires many tests at a number of different loads which is quite time consuming and it requires the same coatings with different thickness which is not economic for practical application. It is also important to note that the $W_{irr}$ method is only valid in the case of a fracture-related feature in $P$-$\delta$ curve otherwise no obvious characteristic change in work is observed which invalidates the method (see the example for inorganic-organic coating on glass in [27]). Another

approach based on plotting irreversible work versus load has been proposed [28]. It was suggested that the position of the $W_{irr}$ jumps (i.e. $\Delta W_{irr}$) on the $W_{irr}$-$P$ curve correlates with the evidence of the first crack in micrographs, and reasonable results for toughness were reported. However, there are lots of events in a plot of $W_{irr}$-$P$ after the critical load (see Ref. [28]) and it is difficult to associate each with a particular fracture event. Therefore, the method actually depends on detecting the first event associated with a measurable crack dimension which is not be easily done; the extension of the cracks as the load increases cannot be directly monitored and only their final positions at the end of the test are known in most cases.

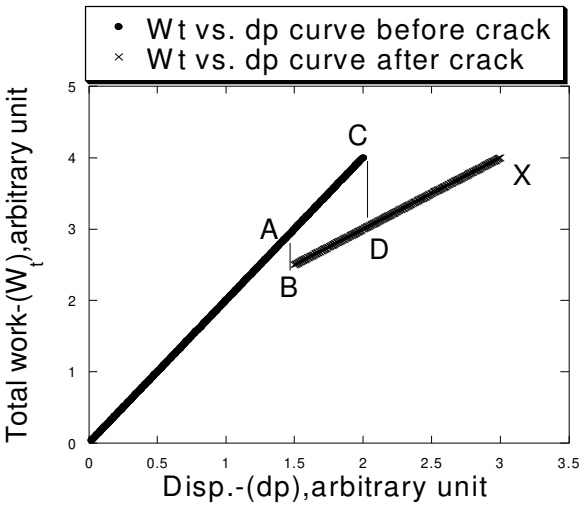


**Figure 3.** Schematic of the extrapolated total work vs. displacement curve before and after cracking to determine the fracture dissipated energy CD-AB.

## 3. Experimental

It is well-known that the threshold for cracking can be dramatically lowered by using a sharper indenter such as a cube corner tip [20]. In addition to the advantage of reducing the critical load for fracture, at the same penetration the plastic deformation is more confined compared to a Berkovich indenter which can eliminate the influence from the substrate in some circumstances [29]. Therefore, it is preferable to use a cube corner tip when assessing the toughness of thin films.

It is often argued that a step in the load-displacement curve obtained under load control indicates the loss of contact caused by a transient event such as fracture in brittle materials, but it cannot be assumed that the energy dissipated during the displacement excursion is due to the transient event only because of the possible additional permanent deformation associated with it [30]. In contrast, the load drop in a displacement-controlled experiment was argued to be unambiguously related to loss of contact attributed to fracture. More comparisons show that displacement control tests eliminate the additional deformation inherent with fracture [22]. Also, it has been argued that the displacement control tests will be more sensitive to the fracture initiation [31]. Therefore, displacement control was used throughout in this study.

The low load tests were carried out using a Hysitron Triboindenter fitted with a cube corner tip (tip radius is 40nm when new). It has been suggested that many coatings

flex elastically up to displacements approximately equal to the coating thickness when the onset of fracture may occur [3, 32]. Therefore, the maximum displacement control set point is 400nm which is equal to the thickness of the thick top layer (except for the sample with a 240nm indium tin oxide (ITO) coating). The tests were performed at range of maximum penetration depths from 40nm to 400nm. The loading rates were varied from 5nm/s (for low penetration) to 40nm/s (for high penetration). The hold time at peak load for each case is 5 seconds. In-situ AFM was used to obtain the fracture dimensions.

In order to gain more insight about the fracture behaviour of the coated glass, nanoindentation tests were also performed using a blunt tip (Berkovich tip with tip end radius of ~250nm) using a Nanoindenter II $^{TM}$ (Nano Instruments, Knoxville, TN, USA). A wide range of loads was applied to each sample (from 10mN to 500mN). The loading rate was 50nm/s for peak loads bigger than 300mN and 10nm/s was used for lower loads. In order to measure the fracture dimensions, off-line SEM (Camscan) and AFM (Park M5) were used.

The coatings investigated here are the main ceramic components of solar control coatings such as ZnO, $SnO_2$, and $TiO_xN_y$ produced by magnetron sputtering with the same process parameters as are used in a commercial coating stack (Pilkington Optitherm). The coated system tested is a multilayer stack consisting of very thin layers of coating materials deposited with the same architecture and deposition conditions as in a commercial solar control coating, capped with a 400nm thick layer of each individual constituent material for fracture assessment. Descriptions of the samples are provided in Table 1. The hardness, H, and elastic modulus, E, values for the coatings were obtained by extrapolating the measured values determined by the Oliver and Pharr method at a range of maximum displacements [33].The H/E ratio of the main components of the solar control coating architecture investigated together with the substrate are given in Table 2.

**Table 1**. Samples of a typical sputtered solar control coating stopped after each different layer in the multilayer stack with the final thickness increased to 400nm. N.B., this leads to spallation of ITO due to high residual stress so an extra sample was produced with a 240nm thickness top layer which does not spall.

| |
|---|
| **Sample 1:** 400nm $TiO_xN_y$ on substrate glass |
| **Sample 2:** 400nm $TiO_xN_y$ on 40nm $SnO_2$on 5nm ITO on 10nm Ag on 10nm ZnO on 20nm $TiO_xN_y$ on substrate glass |
| **Sample 3:** 240nm ITO on 10nm Ag on 10nm ZnO on 20nm $TiO_xN_y$ on substrate glass |
| **Sample 4:** 400nm ITO on 10nm Ag on 10nm ZnO on 20nm $TiO_xN_y$ on substrate glass |
| **Sample 5:** 400nm $SnO_2$ on 5nm ITO on 10nm Ag on 10nm ZnO on 20nm on $TiO_xN_y$ substrate glass |
| **Sample 6:** 400nm ZnO on 20nm $TiO_xN_y$ on substrate glass |

**Table 2.** *H/E* ratio of the main components a typical solar control coating and its glass substrate obtained by nanoindentation at maximum loads from 100μN to 1mN load using a well-calibrated sharp cube corner indenter (tip end radius <100nm) [14].

| | $E_r$ (GPa) | $H$ (GPa) | $E_r/H$ |
|---|---|---|---|
| Uncoated soda-lime glass | 79 | 6.5 | 12.2 |
| ZnO coating | 114 | 15 | 7.6 |
| $SnO_2$ coating | 131 | 14 | 9.4 |
| ITO coating | 133 | 12 | 11.1 |
| $TiO_xN_y$ coating | 117 | 9 | 13.0 |

*All the $E$ used in this study is the reduced Young's modulus ,i.e. $E_r$ without the subscript. In the absence of accurate values of Poisson's ratio this is the most accurate way of comparing the coating layers.

## 4. Indentation fracture mechanisms

There are two types of fracture associated with indentations in brittle coated systems:

1. Through-thickness fracture which generally runs normal to the coating/substrate interface for thin coatings but may run at a lower angle to it as the coating thickness increases. Through-thickness fracture is exacerbated by the bending stresses which arise once plastic deformation of the substrate occurs and the coating is bent into the impression or over the material piled-up around it.
2. Interfacial fracture which occurs at or near the coating/substrate interface, or the weakest interface in a multilayer stack. Interfacial detachment may occur around the impression during loading and in the contact zone during unloading.

Once fracture occurs, the properties of the coating/substrate system will be affected. For instance, during a through thickness fracture event in a brittle coated system, the following changes of the mechanical response of the coated system may occur,

(i.) The stiffness of the coating decreases,
(ii.) Plastic deformation of the substrate is more likely or even dominates,
(iii.) Redistribution of the elastic and plastic strain may occur. The stored elastic energy in a cracked coating is released, thus, in the further deformation, this part of coating may be elastically deformed rather than continuing to plastically deform.
(iv.) Any membrane stress is released.

Figure 4 displays the schematic of cross-section of an indentation with through thickness cracking by a sharp tip illustrating the processes which might occur. This has a critical influence on any technique to extract toughness from indentation data as is discussed in the next sections.

### *4.1. In the case of sharp tip*

When a brittle coating on hard substrate is indented by a very sharp tip, say a cube corner indenter, radial cracks easily initiate at the indenter edges. When through-thickness cracking occurs, the compressive stress and membrane stress (in Region I in

Fig.4) in the uncracked coating is released. The stiffness of the cracked coating and its adjacent uncracked coating decreases and more load is supported by the substrate. Thus plastic deformation of the substrate is likely to play an increasing role during further indentation. The cracked coating which was plastically deformed will still support some of the load imposed by indenter; after the stored elastic energy is released by through thickness fracture it may be elastically deformed again prior to carrying on plastic deformation during further indentation. After through-thickness cracking the bending stress caused by conforming to the substrate will also be released. The wedging effect for a sharp tip will enhance the opening displacement of radial cracks.

All these mechanisms will lead to a change in the apparent hardness and modulus of the system during a crack event, thus altering the shape of the indentation load-displacement curve (or the $W_t$-dp curve). It means that it is not realistic to expect that the load-displacement curve or the $W_t$-dp curve after cracking will follow the same rule as the case prior to cracking. Therefore, the second step, i.e. extrapolating the $W_t$-dp curve backward, described in the previous section is essential to account for such deviations. A similar approach cannot be easily be used to separate the load contributions from the different deforming mechanisms. The reason is that the energy can be treated as a simple sum of elastic work, plastic work, fracture dissipated energy plus energy dissipated by heat etc (which is usually neglected) and different contributions may easily be subtracted whilst the failure stress is very much more complex and expressions for each individual mechanism are not always available and cannot be simply added. For instance, it is often the case that a second step in load-displacement curve will lead to a negative value of toughness if a stress-based analysis method is used.

Fig.5 shows the comparison of load-displacement (P-δ) curves between a 400nm $TiO_xN_y$ single layer on glass with peak displacements of 100nm and 400nm. There is no evidence for fracture at the lower penetration but clear load drops are visible in the load-displacement curve for the deeper penetration. There is also some evidence of uplift next to the bigger indent (circled in Figure 5d) which could be evidence for coating detachment since this material does not show appreciable pile-up and the substrate shows neither significant plastic deformation nor the significant constraint of plastic deformation in the coating which would enhance what pile-up there is. The Wt-dp curve corresponding to the load-displacement curve in Fig. 5c is also plotted in Fig. 6. Two significant discontinuities are observed corresponding to events in Fig.5c. Further line profiles have been extracted from Figure 5d and are presented in Figure 7. The depth of the gap at point C as depicted in Fig.7 is about 25nm which is much bigger than the roughness on the coating and the possible roughness of the cube corner tip; it is very common that a cube corner tip is worn when indenting hard materials for even a short period of time. Furthermore, the opening of the gap marked at Point C in Fig.7 is 50nm. Given that the image was made with the tip that made the indentation which is blunt compared to a conventional AFM tip it is unlikely that this feature corresponds to an open crack only. Rather it is likely to be due to the detachment and lateral displacement of the coating. The crack opening is enhanced by the deformation of the relatively soft substrate. To observe cracks by AFM using a blunt tip (such as the indenter used to make the impression here) requires height differences between the material on either side of the crack which is not always observed.

The first event i.e. Event A-B-C in Fig. 5c is accounted for by a radial crack, whilst, the second event, i.e. Event D-E in Fig. 5c is related to interfacial failure. The upthrust in Fig. 5d provides evidence of interfacial failure. The extra linear portion in the unloading curve in Fig. 5c is caused by the rebound of the delaminated coating which implies that the delamination event occurs during the loading half cycle.

For very low load tests, especially for the tests here which are intended to eliminate the substrate influence, it can be expected that fracture due to bending stresses imposed by the plastic deformation of substrate is not significant before other crack modes occur. Further, given the sharp geometry of the cube corner tip (with a small tip end radius as well), the high stress intensity should result in the appearance of radial cracking. Also, it has been argued that the wedging effect is significant for an acute probe [23-24], which makes radial cracking more likely to occur than picture frame cracking. Therefore, although the crack patterns at loads where events are first observed in the load-displacement curves in this study are difficult to directly verify by microscopy such as SEM, in-situ AFM or high resolution off-line AFM, radial fracture following the indenter edges is assumed here as has been routinely observed in SEM studies of high load indents.

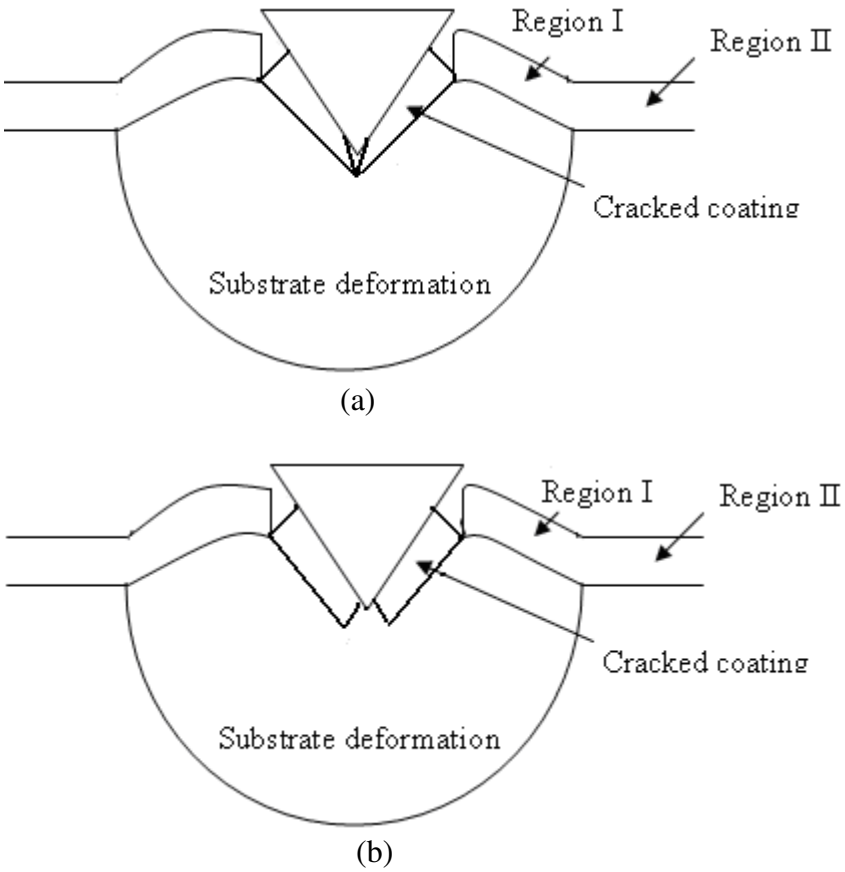


**Figure 4.** Schematic of the cross-section of an indention with through-thickness cracking by a sharp tip. (a) High tensile stress at the wedge tip causes fracture and (b) the bending of the coating around the indenter causes failure. The upthrust of the coating and the plastic deformation of substrate is exaggerated in this figure.

The crack horizontal dimension is assumed equal to the indentation radius (because no evidence of extended radial cracking was observed by in-situ AFM) and the vertical dimension is equal to coating thickness as discussed in the previous section. Since there are three indenter edges, this area must be multiplied by 3 to get the total crack area which assumes uniform fracture around the indentation. The assumption that the crack length is equal to diagonal of impression may not be true but it is reasonable upper limit (giving a lower limit for toughness). For hard brittle coatings on softer substrates, any radial crack is usually confined within the impression. Example are given in Figure 8 where the radial cracks in 1μm fullerene-like $CN_x$ on Cr [34] and titanium nitride coatings on steel are clearly constrained within the indentation. Radial cracks caused by a Vickers indenter in glass during a microindentation test occur during unloading and propagate during the whole unloading cycle. However, for the cube corner indenter, in situ indentation observations found that the radial crack driving force is very small during unloading which results little or no radial crack growth [23].

**Table 3.** The energy release rates and toughness values calculated for the solar control coating components investigated in this study based on the radial through-thickness fracture.

| | Energy release rate of coating $G_{IC}$ ($J/m^2$) calculated by the $W_t$-dp model | Toughness of coating $K_{IC}$ ($MPa\sqrt{m}$) | |
|---|---|---|---|
| | | $W_t$-dp model | Estimated by CIM |
| 400nm $TiO_xN_y$ top layer single layer stack | 24.4 ± 1.4 | 1.8 ± 0.2 | 0.9 ± 0.1 |
| 240nm ITO top layer mutilayer stack | 36.3 ± 8.2 | 2.2 ± 0.3 | 0.9 ± 0.1 |
| 400nm ITO top layer mutilayer stack | 32.7 ± 4.4 | 2.1 ± 0.2 | 0.7 ± 0.1 |
| 400nm $TiO_xN_y$ top layer mutilayer stack | 24.1 ± 7.8 | 1.8 ± 0.2 | 1.0 ± 0.1 |
| 400nm $SnO_2$ top layer mutilayer stack | 29.3 ± 9.8 | 1.9 ± 0.3 | 1.3 ± 0.1 |

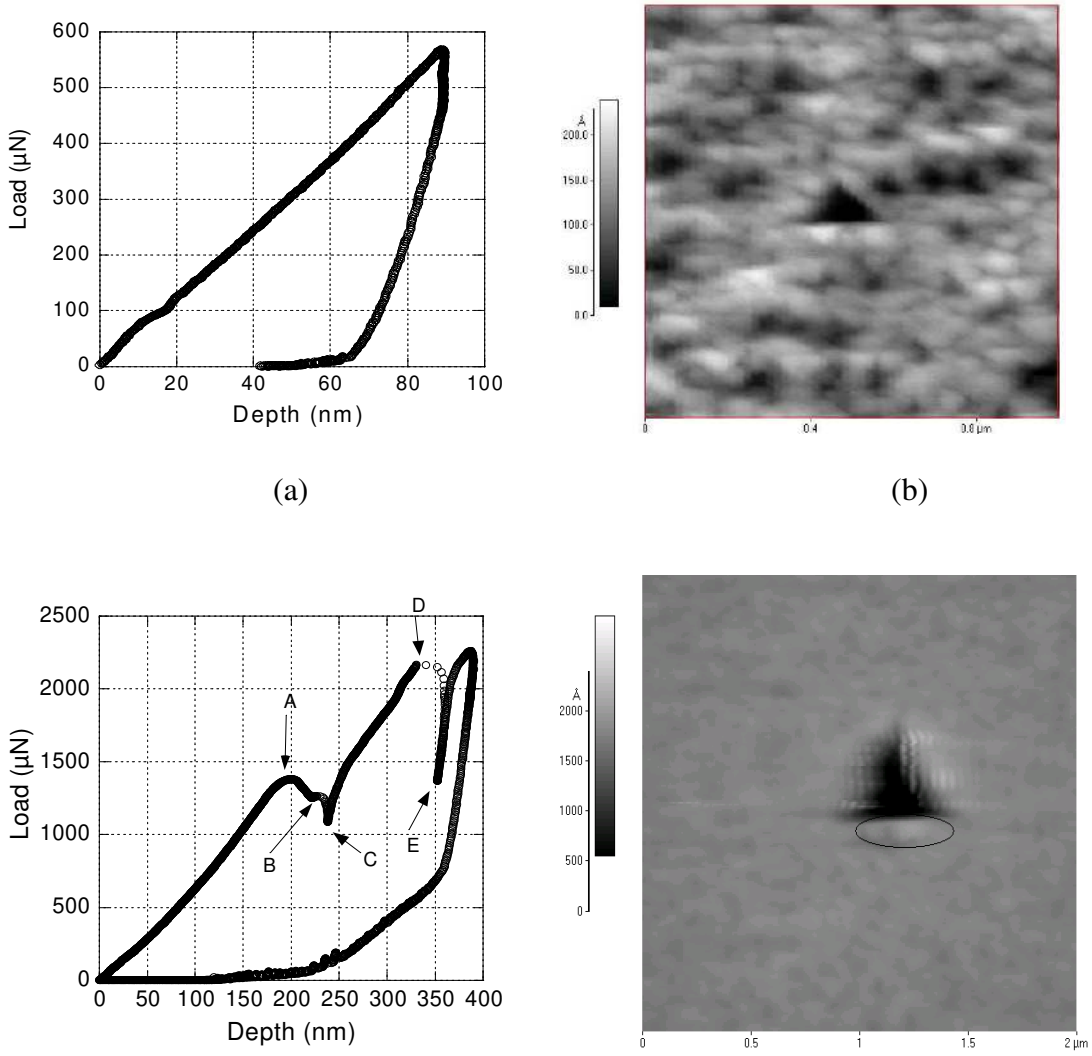


**Figure 5.** (a, c) Load-displacment curves and (b, d) AFM images of a 400nm $TiO_xN_y$ coating on a glass substrate (a, b) without cracks and (c, d) with cracks, respectively. The coating was indented by a cube corner tip under displacement control at 100nm maximum displacement (a, b) and 400nm maximum displacement (c, d). The circle in (d) marks an area of uplift associated with through-thickness and interfacial fracture. In (c), position A is regarded to be the position where plastic deformation extends to the softer substrate which is reasonable since the estimated plastic deformation exceeds 400nm based on the analysis by; points B and C are the start point and end point of through-thickness cracking, respectively; D and E are the start point and end point of interfacial fracture.

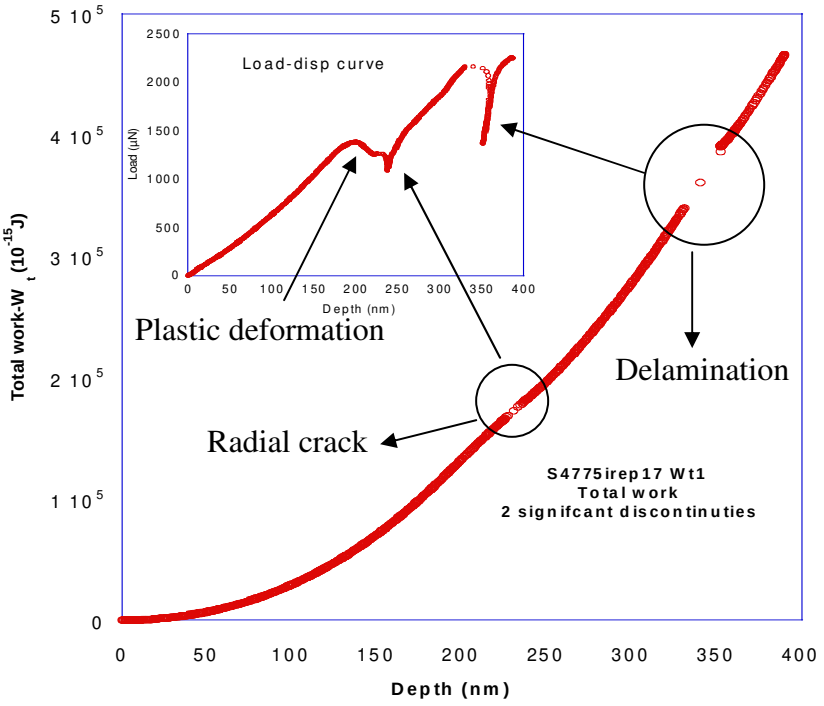


**Figure 6.** Total work versus displacement curve for a 400nm $TiO_xN_y$ coating on glass. Two significant discontinuities are observed. These two events are related to different fracture mechanisms (see text).

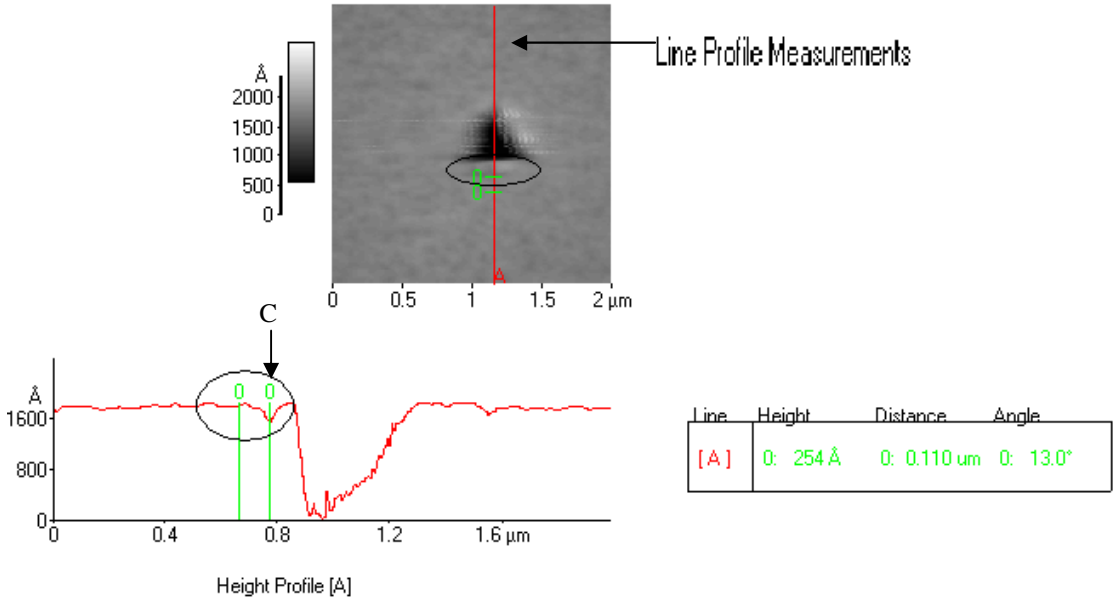


**Figure 7.** AFM line profile measurement corresponding to Fig.5(d). An open through-thickness crack is visible at point C.

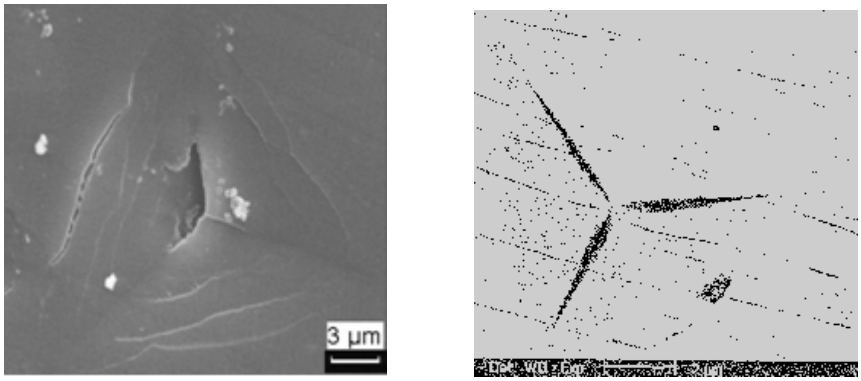


(a) (b)

**Figure 8.** Scanning electron micrographs of (a) a1µm fullerence-like $CN_x$ coating on Cr and (b) a 1µm titanium nitride coating on steel. In both cases it can be seen that the radial cracks following the indenter edges are confined in the indent impression. This is particularly clear in (b).

From Table 3, it can be seen that the results from the wt-dp model are reasonable for the brittle coatings under investigation here whereas the conventional indentation method (CIM) just returns the toughness of the substrate glass in most cases. Although sub-threshold cracking has been investigated elsewhere [35], it requires many tests on a well-documented material to calibrate the constants in the model which is feasible for bulk material but not for thin coatings because their mechanical properties are not usually well known. The contribution from the release of residual stress in the coating is relatively small, (<8%) in this study, unlike in the case of interfacial fracture or radial fracture for very brittle coatings with large residual stress (e.g. [4]). More discussion can be found in [14].

By determining the fracture initiation load the relative toughness can be obtained if it is assumed that the flaw size and distribution is similar. This shows a similar trend to the toughness values calculated in this paper [36].

In order to further verify the model, it has been applied to measurements on different coated systems and data from the literature. For example, an examination was carried out on experimental data from the carbon coatings deposited on Si which were initially used in the development of ld-dp model in the work of Li et al [5–6]. The comparison of the fracture toughness for different carbon coatings on Si determined by ld-dp method and $W_t$-dp method is summarized in Table 4. From Table 4 the toughness of cathodic arc carbon coating on Si determined by the ld-dp method was 10.9MPam$^{1/2}$ [5] which was higher than the toughness (~7.9 MPam$^{1/2}$) of bulk diamond [37]. This is not realistic since a coating is usually more brittle than its bulk form because of the defects within the coating. However the $W_t$- dp method provides the result of 6.2 MPam$^{1/2}$ which is more reliable. The difference in toughness for ion beam carbon coating indented by the conical tip and the cube corner tip obtained by the ld-dp method is about 10%. In contrast, the difference drops to 4% when using the $W_t$-dp method. The overall results of these two carbon coatings are in the range 5.5~6.2 MPam $^{0.5}$ which is identical to the toughness range (5~6MPam $^{0.5}$) of diamond coatings reported in literature [37]. It is reasonable to make such comparison because these coatings are highly cross-linked which is close to the structure of diamond

coatings. The main errors of calculation will result from fracture measurement in the initial paper; the overall errors in the calculations by the $W_t$-dp method will be similar to those in the ld-dp method.

For data taken from sol-gel coating reported in literature, the same procedure was adopted and reasonable results were obtained as well. A few more successful application on others coatings can be found in [25].

By the same method, the energy release rates for interfacial failure for 400nm $TiO_xN_y$/glass, and 240nm ITO multilayer/glass are $30\pm14 J/m^2$ and $19\pm9 J/m^2$, respectively, where the delamination area is assumed to be $\pi c^2$ where c is the delamination radius. It is observed that interfacial failure in the other samples (e.g. the $TiO_xN_y$ coating on glass) occurs at higher load than cracking in the coating; this indicates that the interface toughness is comparable to the coating toughness or greater. The energy release rate for interfacial failure is similar to that for the coating itself, which agrees with the comments above. Experimental observation shows delamination at the edge of the sample prior to the indentation which is caused by the high residual stress in the ITO coating introduced during deposition and the additional stress during glass cutting which confirms the relatively poor interfacial toughness for the 240nm ITO multilayer on glass. It is reasonable to expect that such an interface is weaker than that of the $TiO_xN_y$ coating on glass which does not spall. This is consistent with the calculations here. It may also be expected that the interface is weaker than the ITO coating itself which is also suggested by the calculations here. More details about assessment of interfacial failure will be addressed in next section.

With regard to this method, it is difficult to find a reference bulk material. For typical brittle bulk materials such as soda-lime glass, silicon we have investigated here, no load drops were observed even at the maximum load of 10mN where the radial cracking is well-established. The same result was observed elsewhere when indenting fused silicon [20,38] and glassy carbon [38]. This indicates that the radial cracks do not form in a single event but grow incrementally after initiation as the load increases. The first cracks that form are sufficiently small that they do not lead to a load drop in the P-δ curve under displacement control.

**Table 4** The comparison of toughness of carbon coating deposited on silicon by cathodic arc and ion beam between ld-dp method and $W_t$-dp method.

| | Maximum load, mN | $K_{IC}$, $MPa\sqrt{m}$ | |
|---|---|---|---|
| | | Ld-dp method | $W_t$-dp method |
| Ion beam conical tip | 30 | 5.4 | 5.8 |
| Ion beam cube tip | 22.5 | 4.9 | 6.0 |
| Cathodic arc cube tip | 200 | 10.9 | 6.2 |

*4.2. Fracture behaviour in case of blunt tip*

If picture frame cracking rather than a well-developed radial/median crack pattern is observed during indentation, the conventional indentation method for fracture toughness assessment is not applicable; if the picture-frame fracture does not lead to any excursion in the load-displacement curves or total work vs. displacement curves, the existing energy based models also fail. It is very difficult to apply a stress analysis model in these circumstances since the very complex stress field produced around an indentation is modified by the presence and location of fracture. Complex crack patterns produced during picture-frame cracking are not amenable to simple stress analysis. The question therefore arises can we measure the coating toughness based on picture frame cracking which does not lead to any obvious discontinuities in the load-displacement curve. This section is devoted to answering this question.

*4.2.1 Crack patterns caused by blunt tip*

Except for the sample with a thick cap layer of $TiO_xN_y$, picture-frame cracks were clearly observed in SEM images for all samples when the load is bigger than 200mN. Interfacial detachment was only found in coated glass with a 400nm ITO cap layer which results from the relatively poor adhesion between the cap layer and substrate; this is verified by the observation that a 400nm ITO cap layer will spontaneously delaminate after deposition in some locations as shown in next section.

Fig. 9 displays the picture-frame cracks for a 400nm ZnO cap layer indented at loads in the range of 200mN to 500mN and their associated *P-δ* curves are presented in Fig.10. It is obvious that no excursions resulting from fracture were observed in these load-displacement curves. It is not unusual, for this to occur even for an instrument with excellent feedback control of the displacement. Fig. 11 displays the SEM images of 240nm ITO, 400nm $SnO_2$, and single and multilayer stacks with a cap layer of $TiO_xN_y$ indented with a peak load of 500mN. Well-established picture frame cracks are observed for all coatings except the two $TiO_xN_y$ variants. From Figures 9 and 11, the density of picture-frame cracks for the 240nm ITO multilayer and 400nm $SnO_2$ multilayer is significantly less than for ZnO. It is also obvious that the first picture frame crack in ZnO occurs at a much lower load than the other coatings which may indicate that the ZnO has the lowest toughness. The tin oxide-based coatings show less crack opening displacement compared to the ZnO coating. Evidence of lateral cracking (possibly occurring at the interface) was observed in the 400nm ITO coated sample as shown in Section 5.

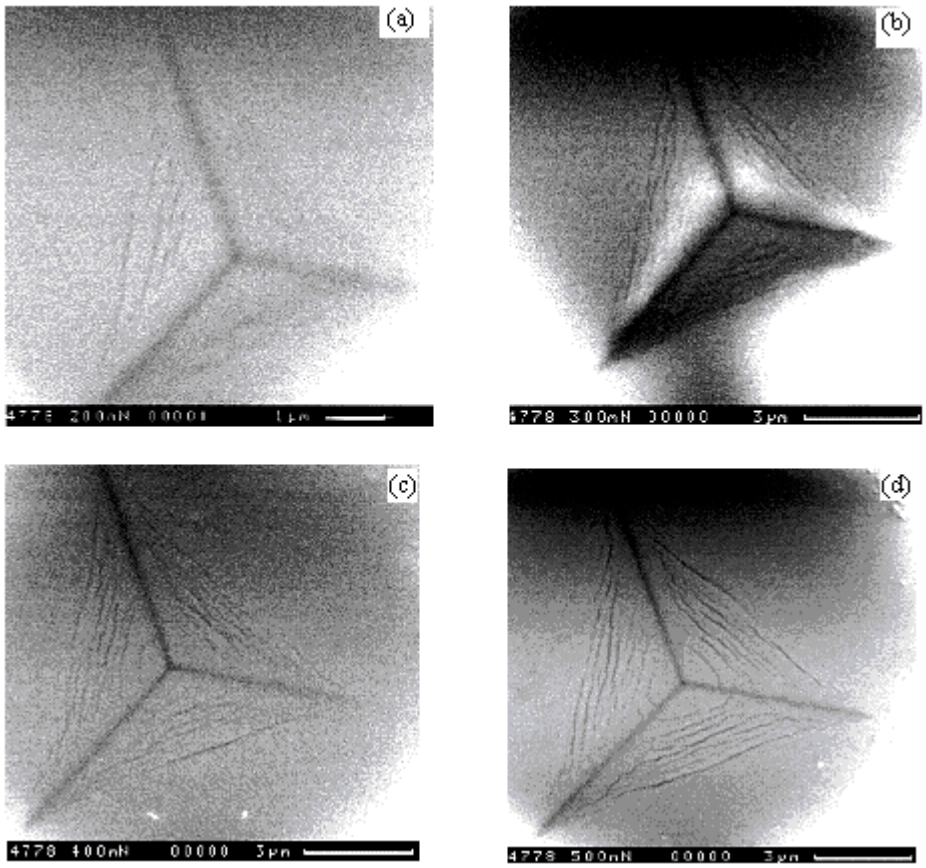


**Figure 9.** SEM (backscattered electron imaging) micrographs showing the picture frame cracks for multilayer coated glass with a 400nm ZnO cap layer. The peak nanoindentation loads are (a) 200mN, (b) 300mN, (c) 400mN, and (d) 500mN, respectively.

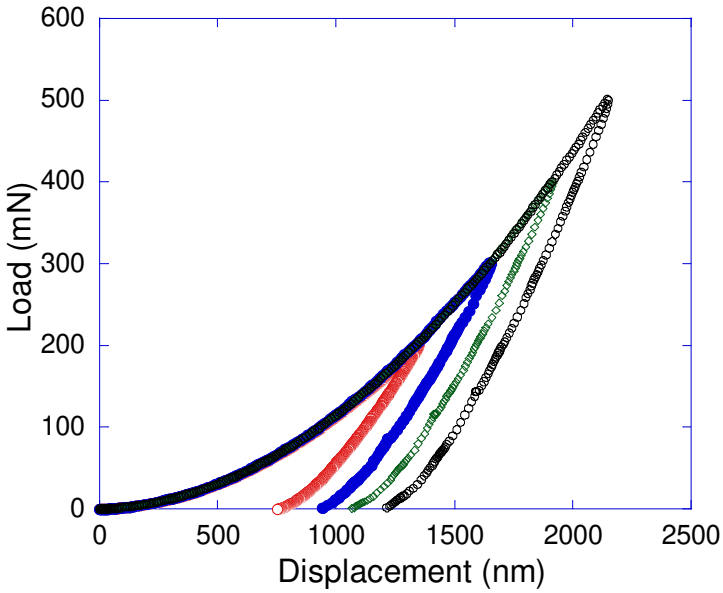


**Figure 10**. The load –displacement curves corresponding to Fig.9. No obvious excursions in the curves were observed.

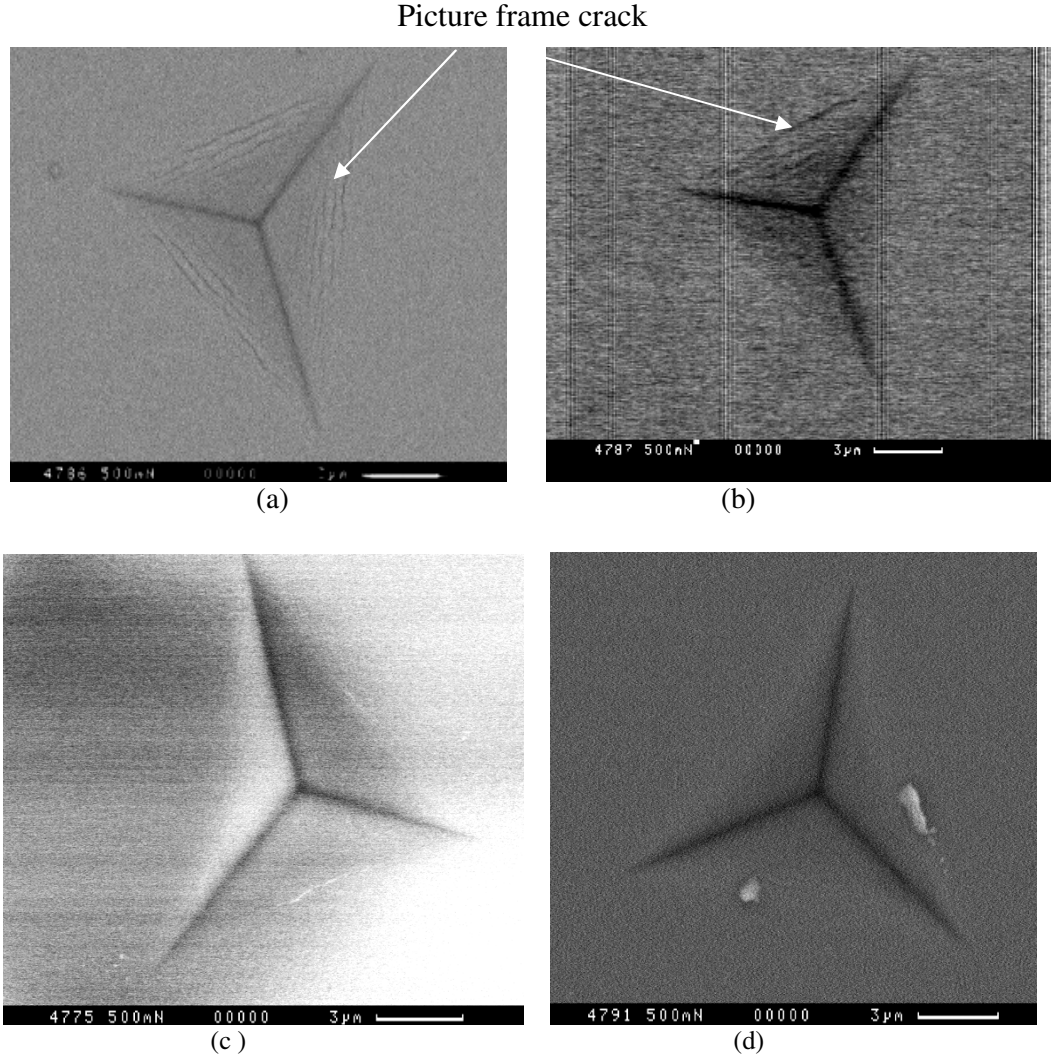


**Figure 11.** SEM micrographs showing the picture frame cracks for multilayer coated glass with a (a) 240nm ITO cap layer, (b) 400nm $SnO_2$, (c) 400nm $TiO_xN_y$ monolayer ,(d) 400nm $TiO_xN_y$ multilayer at 500mN load.

### *4.2.2 Why is there no evidence of picture frame cracking in $TiO_xN_y$ coatings?*

Given the toughness values for the coatings in Table 3 it might be expected that picture frame cracking in $TiO_xN_y$ would be more extensive than is observed. Three possible reasons could account for the observation that no evidence of picture-frame cracking in $TiO_xN_y$ was observed in SEM micrographs.

One is the poor conductivity of $TiO_xN_y$ compared to other coatings which degrades image quality in the SEM and limits the visibility of picture-frame cracks when the opening displacement is small (<20nm). However, even at higher loads the cracking in $TiO_xN_y$ is suppressed so this is unlikely to be the only explanation.

The second reason is that there is a large compressive residual stress in the coating which acts to prevent crack formation and close the cracks once they are formed. Indeed the large compressive stress measured in the tin oxide and ITO coatings (~3GPa determined from the delamination dimensions – see section 5) compared to

the more moderate stress in the ZnO layer (1~2 GPa determined by x-ray diffraction) [39] could explain the differences in the extent of cracking between these samples. However, the stress in the $TiO_xN_y$ layer is very low (200~400MPa determined by sample curvature) [39] and this is not expected to prevent fracture.

The most likely explanation thus depends on the way that the coating/substrate system deforms. If a thin hard coating (usually associated with high yield stress) is well bonded to a softer substrate, the softer substrate will often yield first [40]. In such case, the substrate deformation will add a bending influence on the deformation of the coating. When $\frac{E_f}{H_f} < \frac{E_s}{H_s}$, the plastic zone of the substrate underneath the coating enhances the bending of the coating thus helping to produce the picture-frame cracks and tending to increase the crack opening displacement (see Fig. 12a). This is also the reason that the crack opening displacement (COD) is relatively large in ZnO whose E/H ratio is lowest among all the coatings tested (see Table 2). However, in the reverse case, i.e. $\frac{E_f}{H_f} > \frac{E_s}{H_s}$ (see Fig. 12b), the plastic zone in the substrate does not make much contribution to the bending of the coating so that the COD in $TiO_xN_y$ coatings may be too small to be observed in the SEM used in this study.

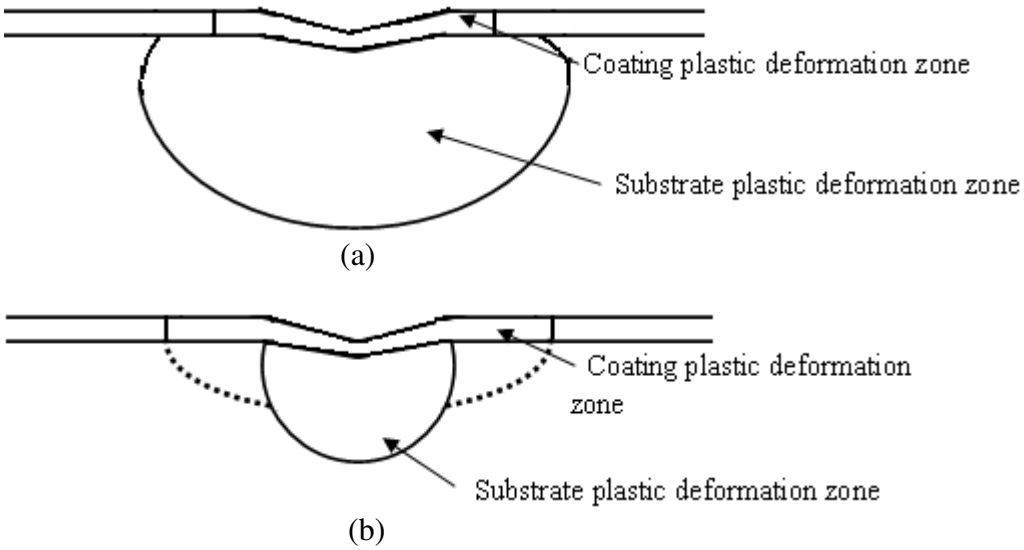


**Figure 12.** Relative plastic zone volumes envisaged for the coated system (a) $E_f/H_f<E_s/H_s$ (b) $E_f/H_f>E_s/H_s$ as proposed by Burnett and Rickerby [40].

*4.2.3 Fracture toughness analysis based on picture frame cracks*

*4.2.3.1 Irreversible work analysis for uncracked materials*

A few workers [41-43] find that there is a linear relationship between the ratio of irreversible work to total work, $W_{irr}/W_t$, and the ratio of final indentation depth to maximum depth, $\delta_f/\delta_m$ for a bulk material without cracks. For example, by combining finite element results and scaling relationships, the following expression was derived by Cheng et al [41],

$$\frac{W_{irr}}{W_t} = (1+\gamma)\frac{\delta_f}{\delta_m} - \gamma \qquad \text{for } \frac{\delta_f}{\delta_m} > 0.4 \qquad (3)$$

For a Berkovich indenter, $\gamma = 0.27$ . In this case, $W_{irr}$ can be also regarded as the plastic work $W_p$.

If it is assumed the load *P* scales displacement squared in the loading curves before cracking and the unloading curves can be fitted by a power law, i.e. $P = A(\delta - \delta_f)^m$ [ 33 ], the following relationship can be obtained [43],

$$\frac{W_P}{W_t} = \frac{3}{m+1}\frac{\delta_f}{\delta_m} - \frac{2-m}{m+1} \qquad (4)$$

Since both equation (3) and the fundamental equations to derive (4) can be verified by finite element simulations for a range of bulk materials, it is reasonable to assume that these two equations are identical, thus giving *m*=1.362.

However, it should be noted that the numerical analysis may not represent the actual behaviour of a bulk material in any particular situation. For example, it is found that there is 3~4% percent deviation when applying this numerical analysis to the soda-lime glass substrate in this study (Fig.13b) which may be caused by the difference between the ideal materials properties used in the numerical simulations and those of real materials. The truncated indenter tip used in practice may also result in some deviation from the numerical result.

If the coated systems have similar *H/E* in both coating and substrate and their *H* and *E* do not deviate much from each other in the composite (i.e. the mismatch of the mechanical properties between coating and substrate is not significant), it is very likely that there will be no slope change in the load-displacement curve after plastic deformation is fully developed in the substrate and *H/E* will not vary with the load. In such a case, the whole coated system can be approximately treated as an equivalent bulk material and the relationships in equations (3) and (4) can also be applied.

For all the samples investigated here it can be shown that $\delta_f/\delta_m > 0.4$ and this meets the requirement for equation (3) to be valid. Here, the work difference between the measured irreversible work and the irreversible work determined from equation (3),

$\Delta W_{irr}$, is less than 4% of the total work and less than 8% of the actual irreversible work (see Fig.13); the difference may be due to microcracks in the glass or intrinsic systematic errors in the experimental data and numerical analysis.

Although no obvious evidence for cracks in the uncoated glass was observed in the SEM images in this study, it cannot be proven that no cracking in the glass occurs under high load tests (>100mN). It has been found that the critical load for cracking in glass indented by a sharp Berkovich indenter is about 20mN with an associated critical flaw size of ~600nm [44]. However, it was also reported elsewhere that the threshold for crack initiation in glass by a Vickers indenter is about 250 to 500mN [20]. The threshold load for fracture may depend on many factors such as the size and distribution of the potential flaws in the glass and the tip radius.

When through-thickness fracture occurs in the coatings, more load is supported by the substrate and coating debris may generate a suitable flaw for fracture initiation in the substrate glass. Therefore, sub-threshold cracking in the substrate glass is expected to contribute to the deviation of $W_{irr}$ from the theoretical value for the coated samples investigated here. Thus, for the calculations in this study, this deviation between experimental and theoretical work for the substrate is subtracted from the measured data for the coated system. It is assumed this systematic deviation is mainly caused by the substrate and it is identical in the different coated systems and the uncoated glass. This assumption is reasonable since the deformation is dominated by substrate under the test conditions used here when high loads (>100mN) are necessary for fracture to occur and the $H$ and $E$ in coatings and substrate do not differ much from each other.

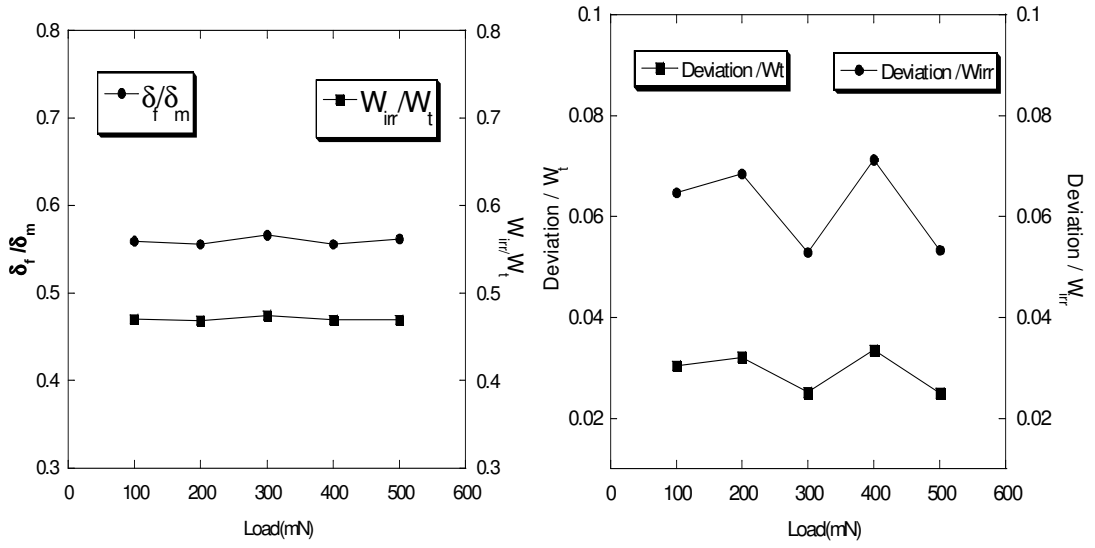


**(a)** **(b)**

**Figure 13.** (a) Plot of $\delta_f/\delta_m$ and $W_{irr}/W_t$ versus load, and (b) plot of $\Delta W_{irr}/W_t$ and $\Delta W_{irr}/W_{irr}$ versus load for uncoated glass at loads from 100mN to 500mN.

The work of indentation can be written as,

$$W_t = W_P + U_{fra} + W_e + W_{other} \quad (5)$$

where $W_t$ is the total work, $W_P$ is work of plastic deformation, $W_e$ is work of elastic deformation, $U_{fra}$ is the fracture dissipated energy, $W_{other}$ represents other items such as the heat dissipated during indentation, work expended in creep and possible microcracks. The sum of all the other items in Eq. (5) except $W_e$ is the irreversible energy $W_{irr}$ (here, we ignore any reversible plastic behaviour). Given an indentation procedure, $W_t$ and $W_e$ can be easily measured. If $W_P$ and $W_{other}$ can be determined, the fracture dissipated energy $U_{fra}$ can be obtained. The following method is one way of achieving this.

The method of irreversible work difference (denoting as $W_{irr}$-$W_p$) is explained as follows.

a) Consider an imaginary load displacement curve with the same plastic work as that for an experimentally measured system.
b) The imaginary load-displacement curve shows no evidence of fracture, i.e. no excursions in the loading or unloading curve which lead to an increase indenter displacement at a fixed load on loading. This will be compared with the experimental data which shows evidence of cracking.
c) Assume that the influence of cracking on the mechanical properties of the whole coated system after cracking applies to the whole loading part of the experimental curve, i.e. averaging the crack influence on the plastic and elastic deformation over the whole loading cycle. This is a reasonable assumption since *E/H* remains almost constant despite the presence of fracture in the case that no excursion and no slope change in the *P*-$\delta$ curve is observed.
d) In such a case the coated system can be treated as equivalent to a bulk material.
e) Ignoring the energy dissipated by heat etc, $W_t = W_P + U_{fra} + W_e$. The fraction of plastic work remains the same as in the equivalent bulk materials i.e. $W_t = W_P + W_e^{'}$ (where $W_e^{'} = U_{fra} + W_e$ , the hypothesis is to turn the fracture dissipated energy back into the stored elastic energy). The total work does not change because fracture only plays a role in converting some stored elastic energy into irreversible work under displacement control tests.

For the equivalent bulk material constructed by this method, the work of plastic deformation can be approximately determined by equation (3). For best accuracy, the deviation introduced into $W_{irr}$ by microcracking in the substrate is subtracted; this correction is determined by calibration tests on uncracked samples. Thus $U_{fra}$ can be obtained, which represents the dissipated energy used to create new crack surface. The approach can separate the influence of elastic-plastic deformation mechanisms from fracture given coated systems with features similar to what has been described here (i.e. similar *E/H* to the substrate). It needs to be emphasised that the fracture must

not make any contribution to the total work under displacement control. The contribution of fracture is to convert part of $W_e$ into $W_{irr.}$

The coating toughness is then given by,

$$K_{IC} = \sqrt{\frac{U_{fra} E}{(1-\nu^2) A_{fra}}} \tag{6}$$

where $\nu$ and E are the Poisson's ratio and Young's modulus of coating, respectively. $A_{fra}$ is the total area of fracture. In this study, $\nu$=0.25 is used in the absence of better data for the coatings of interest.

Assuming that crack initiation can be described by a critical strain criterion, it can be expected that the picture frame crack spacing is uniform [45]. Provided that picture frame cracking is well established and the outer picture-frame crack is very much bigger than the initial one, it can be shown that the total fracture area of the picture frame cracks is approximately given by,

$$A_{fra} = \frac{3a^2}{2s} t \tag{7}$$

where $a$ is the radial dimension of the indentation, $s$ is the spacing between the cracks as shown in Figure 14 and $t$ is the coating thickness.

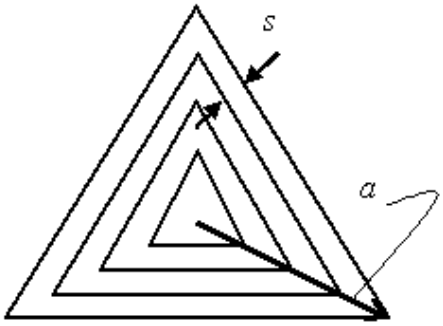


**Figure 14.** Schematic of the picture-frame crack geometry induced by a Berkovich indenter.

The same approach can also be used to assess interfacial fracture toughness providing that the area of interfacial fracture is known. For a circular interfacial crack, the area is given by,

$$A_{\text{int}} = \pi c_R^2 \tag{8}$$

where $C_R$ is the measured interfacial crack radius.

*4.2.3.2 Toughness values of the coatings by $W_{irr}$-$W_p$ method*

From Table 5, the toughness of the ZnO coating is lowest which agrees with the argument in Section 4.2.3.1. Previous tests [46] show that the critical loads for the first acoustic emission (AE) event well after plastic deformation initiation in ZnO and $SnO_2$ are similar, which implies that their toughness will be similar if it is assumed that the flaw size distribution is similar which is also consistent to the data in Table 5. The toughness of the ZnO cap layer determined here is around $1.1 \pm 0.2\ MPa\sqrt{m}$, which is compared to the results in the literature such as $0.8 \pm 0.11\ MPa\sqrt{m}$ [47] for ZnO powder and $1.4\ MPa\sqrt{m}$ for bulk ZnO [48]. The toughness values for the tin oxide-based coatings are similar to those obtained by the $W_t$-dp method (Table 3). The toughness error for ITO is relatively big which is probably due to the high residual stress and defects in the coating. The energy release rate and toughness obtained at various loads for the samples are displayed in Fig.15. The values do not vary much with load which indicates that the model presented here is reasonable. The method has also been applied to radial cracking in bulk materials such as glass and SiC and reasonable results are obtained [22].

When dealing with interfacial toughness, the Young's modulus of the coating in Eq.(6) is replaced by the interfacial modulus defined by Hutchinson and Suo [49] ,

$$\frac{1}{E_{\text{int}}} = \frac{1}{2}\left(\frac{1}{E_c} + \frac{1}{E_s}\right) \tag{9}$$

where $E_c$ and $E_s$ are the Young's modulus of coating and substrate, respectively. Here, the $E_s$ is the effective substrate modulus consisting of contributions from the substrate glass and the other thin layers underneath the cap layer which is determined by the model developed by Bull et al [50-52]. The interfacial toughness is $0.64 \pm 0.07$ $MPam^{1/2}$.

It should be pointed out that if the fracture dissipated energy is as small as the difference of measured and calculated $W_{irr}$, this method will break down since measurement errors will then dominate the calculation.

There is a question as to whether the measured toughness is indenter tip-shape dependent. Li et al [6] found that the measured toughness of carbon coatings is almost identical when using a cube corner tip with sharp edges and its equivalent conical tip. It is also reported elsewhere that there is no tip-shape dependent behaviour in glass and many other brittle materials when comparing the toughness determined by a Vickers indenter [7–9], a Berkovich indenter [53], a cube corner indenter [20] or even a spherical indenter [54-55]. Thus it can be assumed that toughness is independent of indenter shape with reasonable reliability. Furthermore, there is no obvious difference in the measured toughness based on different cracking patterns. For example, for a cone crack produced by a spherical tip, or radial or lateral cracking caused by a sharp tip in glass, the measured toughness is identical. For coatings, Malzbender et al found

that the toughness of the sol-gel coatings in [12,26] is the same based on radial cracking or chipping.

**Table 5.** The energy release rate and toughness of the coatings determined from picture-frame cracking in the case where there is no excursion in the nanoindentation load-displacement curve.

| | Spacing (nm) | Young's Modulus (GPa) | *Energy release rate ($J/m^2$) | *Toughness ($MPam^{0.5}$) |
|---|---|---|---|---|
| 400nm ZnO cap layer | 239 ± 28 | 117 | 10.3 ± 3.8 | 1.1 ± 0.2 |
| 400nm $SnO_2$ cap layer | 412 ± 54 | 133 | 19.9 ± 6.3 | 1.6 ± 0.3 |
| 240nm ITO cap layer | 313 ± 30 | 131 | 39.4 ± 15.9 | 2.2 ± 0.5 |

*Both energy release rate and toughness is the mean value under the loads from 200mN to 500mN.

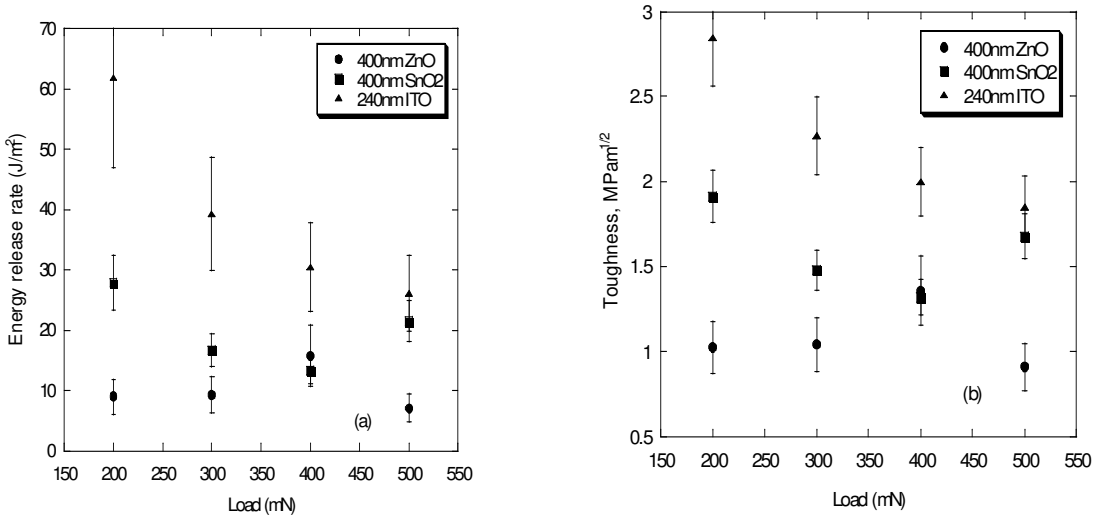


**(a)** **(b)**

**Figure 15**. Plot of (a) energy release rate and (b) toughness for ZnO, $SnO_2$ and ITO cap layers measured by nanoindentation under different maximum applied loads..

## 5. Adhesion assessment

Many indentation models and techniques [e.g. 4, 26, 56-61] have been developed to estimate the interfacial toughness. Most of them either require special experimental techniques which are expensive or restricted to certain coated systems or deal with well-extended delamination (blistering) which may not always be observed. Those methods cannot be easily applied to the interfacial failure observed in this study since the adhesion of the coatings is very good. Therefore, new approaches are developed in this section that can be extended to the coated systems which display similar fracture mechanisms.

*5.1. Extra linear recovery*

Under certain conditions, i.e. rebound after delamination leading to extra linear recovery in the unloading part of the P-δ curve, the adhesion may be assessed by a different method. The linear part (as shown in Fig.16a) occurring near the end of unloading procedure is believed to be accounted for by rebounding of the detached coating during unloading. A model based on elastic equilibrium and the solution for unloading of a centrally loaded disc to assess debonding was proposed by Hainsworth et al. [62]. It was assumed the fracture dissipated energy associated with debonding equals the elastic energy stored in the flexed annular coating segment while ignoring the extra recovery area in the unloading curve. Thus, the energy dissipated by debonding is given by,

$$W_d = W_f = \frac{2\pi E t^3 (\delta_m - \delta_r)^2}{3C_R^2} \tag{10}$$

$$G_{\text{int}} = \frac{W_d}{\pi C_R^2} = \frac{2Et^3(\delta_m - \delta_r)^2}{3C_R^4} \tag{11}$$

However, this model dramatically overestimates the interfacial toughness. For example, for a 4μm TiN/ZrN multilayer on steel indented at 500mN, the calculated $G_{int}$ =173 to 716J/m$^2$ from a debonding length of 5~7 μm which is larger than results determined using other approaches for the same samples (~50J/m$^2$). In addition, it is extremely sensitive to the measured debonding length since the exponent $C_R$ in Eq.(11) is 4. When applying this method to the ceramic coatings in this study, it gives around 20000 J/m$^2$ for 400nm $TiO_xN_y$ and 240nm ITO, which is clearly unrealistic. Therefore, an alternative approach is required.

The mechanism of failure can be explained as follows (see Figure 17). The coating underneath the indenter deflects into the impression in the plastically deformed substrate under load, causing bending stress at the edges of the contact and buckling failure outside the contact during loading if the adhesion is poor. However, the compressive stress beneath the tip causes the coating within the region A-A (see Fig.16) to remain pressed against the substrate. During unloading the coating is detached from the substrate (with a crack radius of $C_R$) and behaves like a spring, pushing the indenter out of the impression and generating load at lower depths than normal elastic unloading. The area of debonding during unloading is given by $\pi C_R^2$ as previously. The case where detachment occurs on loading (Fig. 17b) is difficult to analyse as the energy consumed in fracture on loading is not easy to determine. However, for the samples investigated here the adhesion is good and this does not occur so the geometry is Fig16a is assumed in this study.

To determine the energy to create the debonded area it is necessary to extrapolate the initial part of the unloading curve before the transition point when the effect of detachment is visible to the completely unloaded position. The difference between the extrapolated unloading curve and the actual unloading curve can be regarded as an

approximation of the fracture dissipated energy for delamination (see the crosshatched area in Figure 16a).

For the coated glasses in this study, this approach gives 79.7 ±17.6 J/m$^2$ for the $TiO_xN_y$ / glass interface, thus the interfacial toughness is approximately 2.8±0.3 MPam$^{1/2}$ (using to Equations (10) and (11)). For the ITO/ZnO/Ag interface, the values of fracture dissipated energy and toughness are 35.8 ±14.1 J/m$^2$, and 1.9±0.3 MPam$^{1/2}$, respectively. These results agree reasonably with those determined by a different method (i.e. $W_t$-dp) in the previous section. Further, the method presented here gives fracture dissipated energy values of 32 – 64 J/m$^2$ for TiN/ZrN which is more reasonable for a ceramic/metal interface than the results of the method of Hainsworth et al.

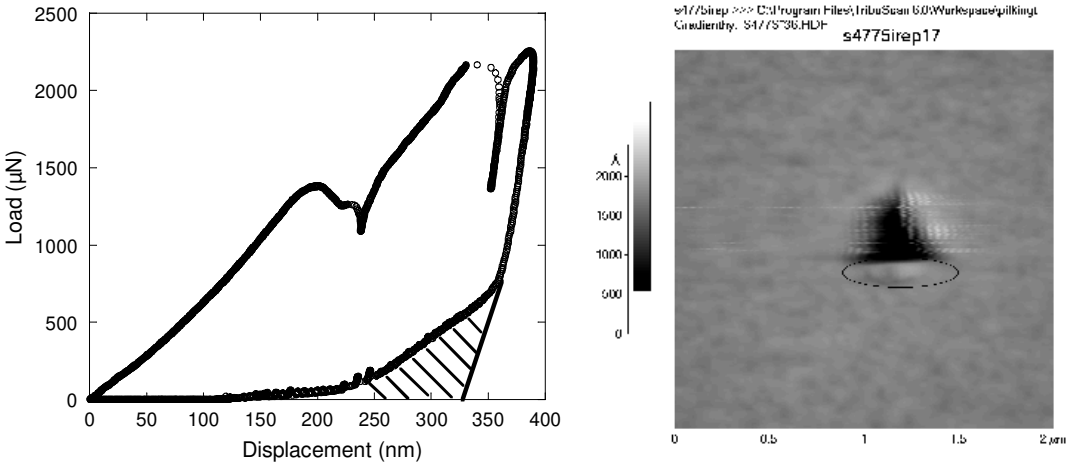


**(a)** **(b)**

**Figure 16.** (a) Extra linear elastic recovery in the load-displacement curve is observed during unloading for a 400nm $TiO_xN_y$ coating on commercial soda-lime glass and (b) its corresponding AFM image.

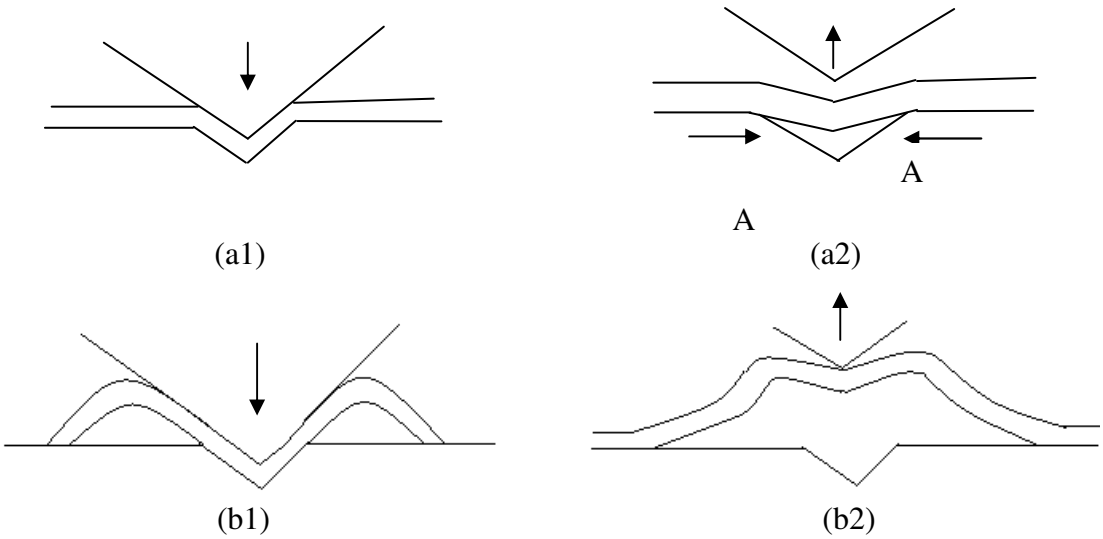


**Figure 17.** Schematic of the rebound of the detached material on unloading (a) good adhesion and (b) poor adhesion. The coating within the region A-A is involved in short-range rebounding as shown in Fig.16.

The reason that the model by Hainsworth et al significantly overestimates the values of interfacial toughness is that the stored elastic energy $U_e$ in the cracked coating segment has been at least partly released by through-thickness cracking prior to debonding. If the release of elastic energy in the coating is what causes detachment and the buckling of the coating then the work done pushing the indenter out should be the same as this. The extra recovery work is assumed to be equal to the energy to create the delamination area (excluding the effects of residual stress in the film) but some other energy dissipation mechanisms may also contribute (plasticity around the crack tip, microcracks, energy stored in bending) which will limit the accuracy of the result.

### *5.2. Lateral crack induced interfacial failure*

The models above deal with the blister formation or delamination, while, interfacial failure can be also caused by a lateral crack occurring at the interface or adjacent to interface in a coating/substrate system.

Based on the expanding spherical cavity model as used in the analysis of the radial/median crack pattern [7,9] and a simple plate theory, Marshall et al [63] proposed a model to relate the toughness of brittle bulk materials to the threshold lateral fracture load and other material parameters giving,

$$K_c^4 = \frac{P_0 A_0^2}{\delta_0}(\cot\theta)^{\frac{2}{3}}\left(\frac{H^4}{E}\right) \qquad (12)$$

Where $P_0$ is threshold load for lateral cracking; $A_0$ and $\delta_0$ are dimensionless constants ($A_0$ =3/4 and $\delta_0$ =1200) and θ is the half-included angle for the indenter.

Under certain circumstances, this method can be extended to assess the interfacial failure of a coated system. It is necessary that the scale of plastic deformation associated with the impression is comparable with the thickness of the coating and that the lateral crack occurs at an interface with poor toughness compared to the coating and the substrate.

For the coated glass and glass substrate investigated here, lateral cracking was only observed in coated glass capped with a 400nm ITO layer which is the sample with the worst adhesion. The crack observed was shorter than the indentation size (see Fig.18) which indicates that it is neither a lateral crack in the glass substrate nor far-field delamination at the interface. It is reasonable to assume that the critical load for the lateral cracking can be obtained when the plastic deformation zone just reaches the interface. As suggested by Chen and Bull [64], for ceramics the radius of the plastic deformation zone is about five times the residual indent depth. For the indent in Figure 18 the residual depth is around 80nm and thus the critical load is about 3mN. Based on Equation (12), a first approximation for interfacial toughness, $K_{int}$=0.44

$MPam^{1/2}$ (or $G_c$=1.9J/m$^2$), can be obtained, which is a reasonable estimation as discussed in Section 5.3.

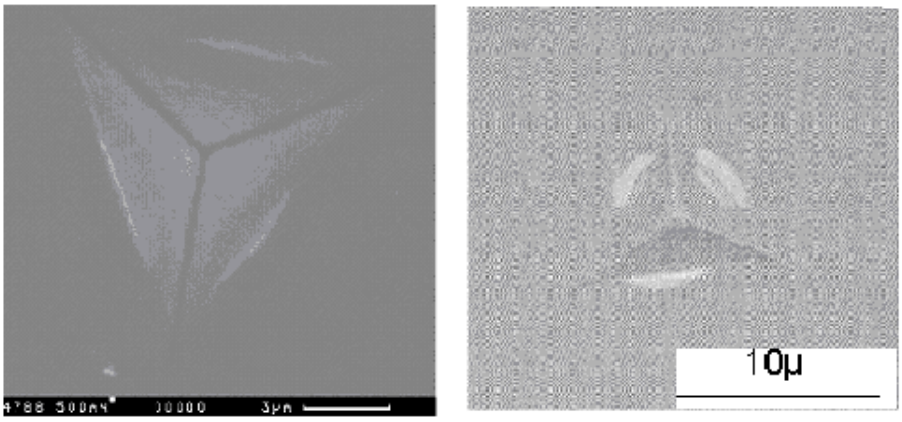


**(a)** **(b)**

**Figure 18.** (a) SEM (secondary electron) micrograph and (b) reflected light micrograph showing lateral cracking for a 400nm ITO cap layer on glass.

*5.3. Comparison of adhesion data from different approaches*

Since spontaneous blistering is observed in some locations on the surface of a 400nm ITO multilayer stack on glass (see Fig.19) an independent measure of adhesion energy is available for comparison with the results produced previously.

Considering the contribution to energy release rate $G_{int}$ for the interface by the critical buckling stress $\sigma_c$ and driving stress $\sigma_r$ of the film (i.e. the residual stress in the coating for a spontaneous buckle) it can be shown that [49],

$$G_{\text{int}} = \left[\frac{(1-\nu^2)t}{2E}\right](\sigma_r - \sigma_c)(\sigma_r + 3\sigma_c) \tag{13a}$$

Where $\sigma_c = \frac{kE}{12(1-\nu^2)}\left(\frac{t}{a}\right)^2$ (13b)

$$\sigma_r = \sigma_c\left[c_1\left(\frac{h}{t}\right)^2 + 1\right] \tag{13c}$$

Here $h$ is the bulge height, $a$ is the half of the width of the blister (as shown in Fig.20), $c_1$=0.75 and, for a spontaneous blister, $k = \pi^2$. This approach yields 2.7±0.1J/m$^2$ for the adhesion energy, which is of the same order of magnitude as the estimate of 1.9J/m$^2$ determined in the previous section.

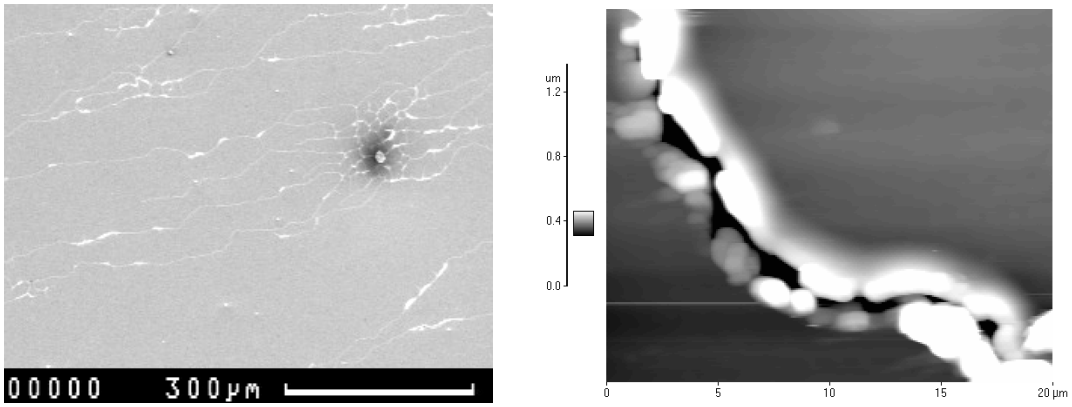


**(a)** **(b)**

**Figure 19.** (a) SEM and (b) AFM image of spontaneous blister in 400nm ITO on glass.

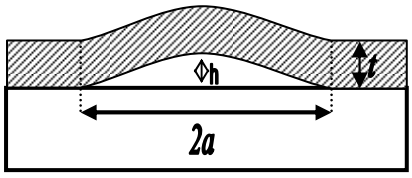


**Figure 20**. Schematic of a cross section of a spontaneous blister in a coated system.

Using Double cantilever beam (DCB) testing, Barthel et al [65] obtained the adhesion energy of 1.4~2.8 J/m$^2$ for a Glass/ZnO ($TiO_2$ or $SnO_2$)/Ag/ZnO (each individual layer thinner than 20nm) stack with the crack path at the ZnO/Ag interface. Density-functional theory calculations [66] in the absence of mechanical energy dissipation at the ZnO/Ag interface provide similar results. Barthel et al [65] stated that that the adhesion energy between $SnO_2$ (or $TiO_2$) and Ag may be at least 50% higher than that of ZnO/Ag for the similar layer stack on glass. The weak interface in this study is one with silver - either Ag/ZnO or Ag/ITO but precisely where failure occurs is difficult to verify in the absence of good transmission electron microscopy images. However, no matter which interface really fails (either ITO/Ag or Ag/ZnO) the value of $G_{int}$ obtained for the ITO/Ag/ZnO interface here based on spontaneous blistering agrees very well with the results by DCB for the similar coating stack reported in the literature. That the ZnO/Ag interface is the weakest and can fail due to residual stress after sputter deposition has been verified by TEM [39].

For the delamination produced by a sharp cube corner indenter analysed by the $W_t$-dp method, the adhesion energy is between 10 to 28J/m$^2$ which overestimates the true adhesion energy due to the inevitable plastic deformation associated with the delamination during loading. The adhesion energy assessed by extra linear elastic recovery for such a coating stack is about 20 to 40J/m$^2$ which again overestimates the interfacial toughness because only part of stored elastic energy drives crack propagation and the fraction is unknown. However, these two methods are useful for qualitative comparison.

The toughness of the coating and the interface toughness may be dependent on coating thickness as in the case of sol-gel organic-inorganic coatings with the thickness from 1.7 to 6.3μm reported by Malzbender et al [26] . In this case, the thinner the coating the bigger coating toughness and interface toughness despite the invariant elastic modulus for these coatings. An approximately linear relationship between coating toughness and thickness was observed. This is probably related to residual stress and flaw size. However, it is also reported elsewhere [12] for similar sol-gel coatings the coating thickness has an almost negligible influence on coating toughness but it significantly affects the interface toughness. That the interface toughness of most coatings is found to be strongly dependent on coating thickness is well-documented and summarized in [61, 67-70]. The main reason that the interface toughness will change with the thickness is due to the residual stress in the coatings; in such cases the detachment is driven by the elastic energy stored in the residually stressed coating which can be released to drive fracture. This increases with coating thickness.

## 6. Conclusions

The different fracture mechanisms which occur in very thin coatings during nanoindentation using a sharp or blunt indenter have been analysed in this study to obtain reliable values for coating toughness. Radial cracks are more likely to occur at low loads when the tip is sharp, while picture-frame cracks form at higher loads or when a blunt tip is used. At the same impression size the picture frame crack density may be an indicator of toughness. The methods developed here provide a route to determine coating toughness by energy-based models whether there are fracture-related features in the load-displacement curve or not. In addition, the analysis of the extra linear recovery during unloading can be used to give a qualitative assessment of adhesion energy which is broadly in agreement with results obtained from lateral crack propagation and spontaneous buckle formation.

Since it is not always possible to generate a particular type of fracture for a given coating/substrate system a range of analysis methods are necessary to extract coating toughness. Approaches based on measurement of energy-dissipation routinely give more reliable results than those based on stress analysis because of the complexity of the stress field around an indentation and the manner in which it is modified by fracture. However, it is essential to correct for all other sources of energy dissipation during indentation if reliable toughness data is to be extracted.

## ACKNOWLEDGEMENTS

This research was supported by The Engineering and Physical Sciences Research Council (EPSRC) through the multiscale modelling initiative.

## References


1. Xie, Z.H, Munroe, P.R, McGrouther, D, Singh, R.K, Hoffman. M (2006), Three-dimensional study of indentation-induced cracks in an amorphous carbon coating on a steel substrate, Journal of Materials Research, **21**, 2600-2605

2. Ma, L.W, Cairney, J.M, Hoffman, M.J, Munroe, P.R. (2006), Deformation and fracture of TiN and TiAlN coatings on a steel substrate during nanoindentation, Surf. Coat. & Tech. **200**, 3518-3526.

3. McGurk, M. R. (1997),, An exploration of contact deformation mechanisms in thin hard coated systems, Ph.D Thesis, University of Newcastle, UK.

4. den Toonder, J., Malzbender, H., de With, G. and Balkenende, R. (2002) Fracture toughness and adhesion energy of sol-gel coatings on glass, Journal of Materials Research, **17**, 224-233.

5. Li, X. D., Diao, D. F. and Bhushan, B. (1997) Fracture mechanisms of thin amorphous carbon films in nanoindentation, Acta Materialia, **45**, 4453-4461.

6. Li, X. D. and Bhushan, B. (1998) Measurement of fracture toughness of ultra-thin amorphous carbon films, Thin Solid Films, **315**, 214-221.

7. Lawn, B. R., Evans, A. G. and Marshall, D. B. (1980) Elastic/Plastic Indentation Damage in Ceramics: The Median/Radial Crack System, J. Am. Ceram. Soc., **63**, 574.

8. Cook, R. F. and Pharr, G. M. (1990) Direct Observation and Analysis of Indentation Cracking in Glasses and Ceramics, Journal of the American Ceramic Society, **73**, 787-817.

9. Anstis, G. R., Chantikul, P., Lawn, B. R. and Marshall, D. B. (1981) A Critical-Evaluation of Indentation Techniques for Measuring Fracture-Toughness .1. Direct Crack Measurements, Journal of the American Ceramic Society, **64**, 533-538.

10. Jang, J., Wen, S., Lance, M. I., Anderson, I. M. and Pharr, G. M.(2004) Cracking and Phase transformation in Silicon during nanoindentation, Mater. Res. Soc. Symp.**795**, U8.15.1

11. Marshall, D. B. and Lawn, B. R. (1977) An Indentation Technique for Measuring Stresses in Tempered Glass Surfaces,J. Am. Ceram. Soc., **60**, 86

12. Malzbender, J. and de With, G. (2000) Elastic modulus, hardness and fracture toughness of SiO2-filled methyltrimethoxysilane coatings on glass substrates, Journal of Non-Crystalline Solids, **265**, 51-60.

13. Emiliani, M. L. (1993) Debond Coating Requirements for Brittle-Matrix Composites, Journal of Materials Science, **28**, 5280-5296.

14. Chen, J. and Bull, S. J. (2006) Assessment of the toughness of thin coatings using nanoindentation under displacement control, Thin Solid Films, **494**, 1-7.

15. Laugier, M. T. (1987) Palmqvist Indentation Toughness in WC-Co Composites, Journal of Materials Science Letters, **6**, 897-900.

16. Nihara, K., Morena, R. and Hasselman, D. P. H. (1982) Evaluation of $K_{IC}$ of Brittle Solids by the Indentation Method with Low Crack-to-Indent Ratio, J. Mater. Sci. Lett. , **1**, 13.

17. Scholz, T., Schneider, G. A., Munoz-Saldana, J. and Swain, M. V. (2004) Fracture toughness from submicron derived indentation cracks, Applied Physics Letters, **84**, 3055-3057.

18. Pharr, G. M., Harding, D. S. and Oliver, W. C. (1993) Mechanical Properties and deformation behaviour of materials having ultra-fine microstructure, Kluwer Academic press.

19. Harding, D. S., Oliver, W. C. and Pharr, G. M. (1995) "Cracking During Nanoindentation and Its Use in the Measurement of Fracture Toughness", Materials Research Society Symposium Proceedings **356**, pp. 663-668.

20. Pharr, G. M. (1998) Measurement of mechanical properties by ultra-low load indentation, Materials Science and Engineering A-Structural Materials Properties Microstructure and Processing, **253**, 151-159.

21. Scharf, T. W., Deng, H. and Barnard, J. A. (1997) Mechanical and fracture toughness studies of amorphous SiC-N hard coatings using nanoindentation, Journal of Vacuum Science & Technology a-Vacuum Surfaces and Films, **15**, 963-967.

22. Chen, J., Energy based models to determine fracture toughness of thin coated systems by nanoindentation, Ph.D thesis, 2006 University of Newcastle, UK.

23. Morris, D. J. and Cook, R. F. (2005) Radial fracture during indentation by acute probes: I., Description by an indentation wedging model, International Journal of Fracture, **136**, 237-264.

24. Morris, D. J., Vodnick, A. M. and Cook, R. F. (2005) Radial fracture during indentation by acute probes :II, experimental observations of cube corner and Vickers indentation, International Journal of Fracture, **136**, 265-284.

25. Chen, J. and Bull, S. J. (2006) A new method based on work-displacement curve to assess the toughness of coated system, Mater. Res. Soc. Symp. **890**, Y0202

26. Malzbender, J. and de With, G. (2000) Energy dissipation, fracture toughness and the indentation load-displacement curve of coated materials, Surface & Coatings Technology, **135**, 60-68.

27. Etienne-Calas, S., Duri, A. and Etienne, P. (2004) Fracture study of organic-inorganic coatings using nanoindentation technique, Journal of Non-Crystalline Solids, **344**, 60-65.

28. Nakonechna, O., Cselle, T., Morstein, M. and Karimi, A. (2004) On the behaviour of indentation fracture in TiAlSiN hard thin films, Thin Solid Films, **447**, 406-412.

29. Stein, W. (2005), Private communication

30. Warren, O. L. and Wyrobek, T. J. (2005) Nanomechanical property screening of combinatorial thin-film libraries by nanoindentation, Meas. Sci. Technol., **16**, 100–110.

31. Warren, O. L. (2006), Private communication

32. Page, T. F. and Hainsworth, S. V. (1995) Procedures for the nanoindentation testing of coated systems, Special Publication of the National Institute of Standards & Technology, (Gaitherburg, USA).

33. Oliver, W. C. and Pharr, G. M. (1992) An Improved Technique for Determining Hardness and Elastic Modulus Using Load and Displacement Sensing Indentation Experiments, Journal of Materials Research, **7**, 1564-1583.

34. Palacio, J. F. (2006) Mechanical properties of high performance fullerene-like $CN_x$ coatings assessed by nanoindentation, Ph. D thesis,,University of Newcastle Upon Tyne

35. Jung, Y. G., Pajares, A., Banerjee, R. and Lawn, B. R. (2004) Strength of silicon, sapphire in the subthreshold flaw and glass region, Acta Materialia, **52**, 3459-3466.

*36.* Chen, J. and Bull, S. J., Assessment of the nanoindentation response of brittle coated systems by analysing the loading curves, submitted to Zeitschrift fur Metallkunde, (2006).

37. Field, J. E. and Pickles, C. S. J. (1996) Strength, fracture and friction properties of diamond, Diamond and Related Materials, **5**, 625-634.

38. Field, J. S., Swain, M. V. and Dukino, R. D. (2003) Determination of fracture toughness from the extra penetration produced by indentation-induced pop-in, Journal of Materials Research, **18**, 1412-1419.

39. Warren, P.D, (2007) Private communication

40. Burnett, P. J. and Rickerby, D. S. (1987) The Mechanical-Properties of Wear-Resistant Coatings .1. Modelling of Hardness Behaviour, Thin Solid Films, **148**, 41-50.

41. Cheng, Y. T. and Cheng, C. M. (1998) Scaling approach to conical indentation in elastic-plastic solids with work hardening, Journal of Applied Physics, **84**, 1284-1291.

42. Cheng, Y. T., Li, Z. Y. and Cheng, C. M. (2002) Scaling, relationships for indentation measurements, Philosophical Magazine a-Physics of Condensed Matter Structure Defects and Mechanical Properties, **82**, 1821-1829.

43. Mencik, J. and Swain, M. V. (1994) Micro-Indentation Tests with Pointed Indenters, Materials Forum, **18**, 277-288.

44. Lawn, B. R. and Evans , A. G. (1977) A Model for Crack Initiation in Elastic/Plastic Indentation Fields, J. Mater. Sci., **12**, 2195.

45. Tuck J.R., Korsunsky A.M., (2000) The influence of coating cracking and delamination on the hardness coated systems, Proceedings of 13th Euro Conf on Fracture, (Elsevier Science), Sep 2000, San Sebastian, Spain.

46. Bull, S. J., Arce-Garcia , I., G-Berasategui, R. E. and Page, T. F. (2003) Indentation fracture, acoustic emission and modelling of the mechanical properties of thin ceramics coatings, Proc. Fracture Mechanics VIII, Houston,TX, pp21-42.

47. Mukhopadhyay, A. K., Chaudhuri, M. R., Seal, A., Dalui, S. K., Banerjee, M. and Phani, K. K. (2001) Mechanical characterization of microwave sintered zinc oxide, Bull. Mater. Sci., **24**, 125-128.

48. Ruf, H. and Evans, A. G. (1983) Toughening by monoclinic zirconia, J. Am. Ceram. Soc., 66, 328-332.

49. Hutchinson, J. W. and Suo, Z. (1992) Mixed mode cracking in layered materials, Adv. Appl. Mech., **29**, 63–191.

50. Bull, S. J. (2001) Modelling the hardness response of bulk materials, single and multilayer coatings, Thin Solid Films, **398**, 291-298.

51. Bull, S. J., Berasetegui, E. G. and Page, T. F. (2004) Modelling of the indentation response of coatings and surface treatments, Wear, **256**, 857-866.

52. J. Chen, S.J. Bull, On the relationship between plastic zone radius and maximum depth during nanoindentation, Surface & Coatings Technology, **201** (2006) 4289–4293

53. Lawn, B. R. and Wilshaw, T. R. (1975) *Fracture of Brittle Solids,* Cambridge

University Press, London.

54. Geandier, G., Denis, S. and Mocellin, A., (2003) Float glass fracture toughness determination by Hertzian contact: experiments and analysis, Journal of Non-Crystalline Solids, **318**, 284-295

55. Warren, P. D., (1995) Determining the fracture toughness of brittle materials by Hertzian indentation, Journal of the European Ceramic Society, **15**, 201-207

56. Rosenfeld, L. G., Ritter, J. E., Lardner, T. J. and Lin, M. R. (1990) Use of the Microindentation Technique for Determining Interfacial Fracture Energy, Journal of Applied Physics, **67**, 3291-3296.

57. DeBoer, M. P. and Gerberich, W. W. (1996a) Microwedge indentation of the thin film fine line .1. Mechanics, Acta Materialia, **44**, 3169-3175.

58. DeBoer, M. P. and Gerberich, W. W. (1996b) Microwedge indentation of the thin film fine line .2. Experiment, Acta Materialia, **44**, 3177-3187.

59. Sanchez, J. M., El-Mansy, S.,Sun, B.,Scherban, T.,Fang, N.,Pantuso, D.,Ford, W.,Elizalde, M. R.,Martinez-Esnaola, J. M.,Martin-Meizoso, A.,Gil-Sevillano, J.,Fuentes, M.,Maiz, J.,(1999) Cross-sectional nanoindentation: A new technique for thin film interfacial adhesion characterization, Acta Materialia, **47**,4405-4413

60. Vlassak, J. J., Drory, M. D. and Nix, W. D. (1997) A simple technique for measuring the adhesion of brittle films to ductile substrates with application to diamond-coated titanium, Journal of Materials Research, **12**, 1900-1910.

61. Volinsky, A. A., Moody, N. R. and Gerberich, W. W. (2002) Interfacial toughness measurements for thin films on substrates, Acta Materialia, **50**, 441-466.

62. Hainsworth, S. V., McGurk, M. R. and Page, T. F. (1998) The effect of coating cracking on the indentation response of thin hard-coated systems, Surface & Coatings Technology, **102**, 97-107.

63. Marshall, D. B., Lawn, B. R. and Evans, A. G. (1982) Elastic/Plastic Indentation Damage in Ceramics: The lateral crack system, J. Am. Ceram. Soc., **65**, 561.

64. Chen, J. and Bull, S. J. (2006) A critical examination of the relationship between plastic deformation zone size and Young's modulus to hardness ratio in indentation testing, J. Mater. Res.**21**, 2617-2627

65. Barthel, E., Kerjan, O., Nael, P. and Nadaud, N. (2005) Asymmetric silver to oxide adhesion in multilayers deposited on glass by sputtering, Thin Solid Films **473**, 272- 277.

66. Bristowe, P. and Lin, Z. (2006), Private communication

67. Malzbender, J., With, G. de., (2002) A model to determine the interfacial fracture toughness for chipped coatings, Surface and Coatings Technology **154**, 21–26

68. Evans, A. G., Hutchinson, J. W. and Wei, Y., (1999) Interface adhesion: effects of plasticity and segregation, Acta Materialia **47,** 4093-4113

69. Reimanis, E. (1998) The measurement of crack front profiles in the fracture of $Au/Al_2O_3$ interfaces ,Acta Materialia **46**, 2479-2484

70. Lipkin, D. M., Clarke, D. R. and Evans, A. G. (1998) Effect of interfacial carbon on adhesion and toughness of gold-sapphire interface. Acta Mater. **46**, 4835–4850